Effect of Elastic Bending Energy on the Emulsification Failure in a Microemulsion

X-L. WU,[1,*] P. TONG,[†] AND J. S. HUANG[‡]

** Department of Physics, University of Pittsburgh, Pittsburgh, Pennsylvania 15260; † Department of Physics, Oklahoma State University, Stillwater, Oklahoma 74078; and ‡ Exxon Research and Engineering Company, Annandale, New Jersey 08801*

Received March 28, 1991; accepted June 12, 1991

Small-angle neutron scattering experiments have been carried out to study the phase stability of a very dilute water-in-oil microemulsion. At the fixed water to surfactant molar ratio of $\omega = 30$, we observed a decrease in the microemulsion droplet radius and an increase in the polydispersity when the dispersed-phase volume fraction, ϕ, was dilute to less than 1%. Upon further dilution to below 0.1%, the droplets disappeared. This suggested that in the concentration range, $0.1\% \leqslant \phi \leqslant 1.0\%$, a single-phase microemulsion was unstable, and a phase separation, known as the emulsification failure, occurred. To understand the interesting phase behavior, we have formulated an analytic solution for the droplet size distribution function for a two-phase microemulsion based on the theory of Borkvec *et al.* (*J. Colloid Interface Sci.* **131,** 366 (1989)). We found that the distribution function attained a simple Gaussian form, and the width of the distribution function was inversely proportional to the renormalized elastic bending energy of the microemulsion droplets. Other features predicted by the theory were also in good agreement with the small-angle neutron scattering measurements.

I. INTRODUCTION

A microemulsion is a thermodynamically stable three-component mixture of oil, water, and surfactant. An example of such a mixture contains decane (oil), water, and sodium di-2-ethylhexylsulfosaccinate (AOT surfactant). For certain compositions of these three components, a homogeneous and optically clear single-phase solution can be obtained at room temperature. Many previous scattering experiments (2, 3) have established that at moderately low dispersed-phase (Water + AOT surfactant) volume fraction, $\phi \geqslant 0.02$, the microemulsion consists of surfactant-coated spherical water droplets dispersed in the oil-continuous medium. The size of the droplets is rather uniform and it is determined by the water to surfactant molar ratio (4, 5). At higher concentrations, there are indications that the microemulsion consists of densely packed droplets which exhibit interesting glassy behaviors (6–8).

In contrast to the extensively studied microemulsions in the above mentioned droplet concentrations, much less is known concerning the structure of such a single-phase microemulsion when it is continuously diluted such that the surfactant concentration is too low to coat all the droplets. In this case the microemulsion will have a phase separation as signified by a precipitation of a water phase from the bulk oil phase. The coexistence of a microemulsion phase with an excess water phase is known as type-II microemulsion. The transition of a single-phase water-in-oil microemulsion to type-II microemulsion is called emulsification failure. A careful study of the microemulsion in this region will not only give us insights about the key factors which control the emulsification process, but also provide a quantitative measurement of thermodynamic parameters, such as the elastic bending energy (9), κ, the spontaneous radius, R_s, and the critical micellar concentration (CMC), X_s^c. Recently, Borkovec *et al.* (1) have proposed a theoretical model to study the phase behavior of the microemulsion in the emulsification failure region. However, there are no prior experimental studies to compare with the theoretical predictions.

In this paper we present an experimental study of this emulsification failure phenomenon using the small-angle neutron scattering (SANS) technique. The system under study was an AOT microemulsion with the fixed water-to-surfactant molar ratio of $\omega \simeq 30$. We found that at high dispersed-phase volume fractions, $\phi \geqslant 1\%$, both the droplet size and the polydispersity remained constant; at the intermediate volume fraction, $0.1\% \leqslant \phi < 1\%$, the microemulsion droplet size decreased and the polydispersity of these droplets increased as the sample was diluted; and at very low volume fractions, $\phi < 0.1\%$, the microemulsion droplets apparently disappeared. The above experimental observation is interesting, particularly for the intermediate concentration range. For fixed water-to-surfactant molar ratio and fixed surfactant monomer concentration (X_s^c) in the oil, dilution decreases the surface-to-volume ratio of the dispersed-phase due to the finite CMC. Therefore, the microemulsion droplet size is expected to increase in the single-phase region. The fact that we observed a reversed behavior in the intermediate concentration range suggests that some of the water molecules were removed from the microemulsion phase and this causes the phase separation. To explain the experimental results quantitatively we have derived an analytic form for the size distribution function in the two-phase region based on a model proposed by Borkovec *et al.* (1). Our calculations showed good agreements between the theory (1) and the experiment, indicating that the theory has captured the essential physics of this three-component microemulsion. More specifically, we found that the elastic bending energy κ was $\sim k_B T$, the spontaneous radius R_s was ~ 60 Å, and the critical micellar mole fraction X_x^c was $\sim 2 \times 10^{-4}$ for our system. We believe that this is the first time R_s has been measured experimentally for this system. It is interesting to observe that the elastic bending energy measured in our static scattering measurement is smaller than that obtained from the dynamic scattering (neutron spin-echo) measurement (10). The difference between the static and dynamic measurements may be explained by the saddle-splay energy, $\bar{\kappa}$, which normalizes both the elastic bending energy, κ, and the spontaneous radius, R_s, as suggested recently by Safran (11). We will show later that in the static measurement one actually measures a renormalized elastic bending energy and a renormalized spontaneous radius. For simplicity we still denote them as κ and R_s, respectively.

In the next section, we will present the theory of Borkovec *et al.* (1) and our own calculations, which we used to interpret our experimental results. The theory of the neutron scattering from polydispersed spherical shells is also briefly reviewed for the purpose of analyzing the scattering data. Section III contains experimental details, including the sample preparation and the neutron scattering measurements. Our results and the interpretations also appear in that section. Finally the work is summarized in Section IV.

II. THEORY

II.1 Thermodynamics of Water-in-Oil Microemulsion

Formation of droplets in a dilute water-in-oil microemulsion can be viewed as an aggregation of water and surfactant monomers. To described this process, Borkovec *et al.* (1) have developed a statistical model which combines features of thermodynamics of mixed micella formation and the established characteristics of the free energy of microemulsion. The predicted phase diagram is shown in Fig. 1. As shown in the figure, for a fixed water to surfactant molar ratio, ω_0, the solution has three different thermodynamic regions depending on the surfactant concentration, X_s. The boundaries between these regions are char-

[1] To whom correspondence should be addressed.

0021-9797/92 $3.00

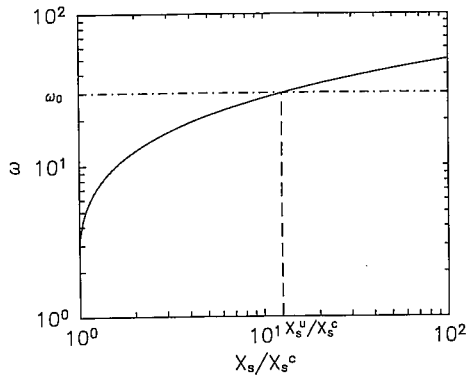

FIG. 1. The emulsification failure phase diagram. Emulsification failure phase boundary is plotted on a log–log scale of the water to surfactant molar ratio ω vs. the reduced surfactant concentration X_s/X_s^c. The solid curve represents the emulsification failure phase boundary. Above this curve the system is in the two-phase region and below this curve the system is in the single-phase region. The horizontal dash–dot line shows $\omega = 30$. The vertical dash line indicates the upper demixing point. As shown in the figure, to produce a single-phase microemulsion one needs more surfactant for larger ω. (See Ref. (1) for more details).

acterized by two surfactant concentrations: the critical micellar concentration (CMC) X_s^c, and the upper demixing concentration X_s^u. (1) For $X_s < X_s^c$, the macroscopic water and oil phases are at coexistence, each saturates with a trace amount of the other components. Because of very low surfactant concentration, they are dissolved as monomers in both the oil and the water phases. No aggregation occurs in this region. (2) For $X_s^c \leqslant X_s \leqslant X_s^u$, water droplets coated by the surfactants start to form. Though the system is still in the two-phase region, known as a type-II microemulsion, the volume of the macroscopic water phase decreases as more and more water molecules become solubilized in the oil phase in the form of droplets as X_s is increased. (3) For $X_s > X_s^u$, all the water is solubilized in the oil phase and a single-phase microemulsion forms.

The above physical picture can be quantitatively described by a distribution function of the aggregation number, N, of surfactant molecules. In terms of the dimensionless radius $\rho = \sqrt{N}$, the elastic bending energy κ, and the spontaneous radius ρ_s, the size distribution function can be written as (1)

$$f(\rho) = \rho^{\nu} e^{-g(\rho)}, \qquad \text{[II.1.1]}$$

where

$$g(\rho) = \xi\rho^2 + \lambda\eta\rho^3 + 8\pi\beta\kappa(1 - \rho/\rho_s)^2 - \beta\Delta\mu_d. \qquad \text{[II.1.2]}$$

Here λ ($\simeq 1.3$) is the volume ratio of surfactant to water molecules (12), β is the reciprocal of k_BT, and $\beta\Delta\mu_d$ is a constant which determines the total number of droplets present in the system. The exponent ν is used to characterize contributions from the entropy of mixing and the thermal undulations of the droplets. Obviously, the size distribution depends on both of these effects, since the former favors more but smaller droplets and the later tends to have a bigger effective radius. Because the dominant contribution to $f(\rho)$ is from the exponential part, the particular value of ν does not affect the final results strongly. On the other hand, in order for the distribution function, $f(\rho)$, to be zero at the origin, ν must be a positive finite number. The calculation below can be easily generalized to any value of ν, but for the simplicity we will take $\nu = 1$, in accordance with Ref. (1) (13). The distribution function, $f(\rho)$, also depends on two other parameters:

$$\xi = \beta\Delta\mu_s - \log x_s, \qquad \text{[II.1.3]}$$

and

$$\eta = \beta\Delta\mu_w - \log x_s, \qquad \text{[II.1.4]}$$

where $\Delta\mu_s$ ($\Delta\mu_w$) is the standard chemical potential difference of surfactant (water) molecules, and x_s (x_w) is the mole fraction of surfactant (water) monomers. Physically, the parameter ξ is the chemical potential difference between a surfactant in the saturated oil/water interfaces and a surfactant dissolved in the oil, and it measures the concentration of free surfactant monomers. The parameter η, on the other hand, is the chemical potential difference between a bulk water molecule and a water molecule dissolved in the oil, and it measures

the concentration of free water monomers. Alternatively, ξ and η can be viewed as Lagrangian multipliers which fix the overall mole fractions of surfactant and water molecules, respectively.

Using the distribution function, $f(\rho)$, the nth moment of the dimensionless radius, ρ, can be defined as

$$\langle \rho^n \rangle = \frac{\int_{\rho_l}^{\infty} d\rho f(\rho)\rho^n}{\int_{\rho_l}^{\infty} d\rho f(\rho)}, \qquad \text{[II.1.5]}$$

where the lower integration limit, ρ_l, denoting the smallest aggregation size, should be taken to be greater than one. Since $\rho = \sqrt{N}$, where N is the surfactant aggregation number, the actual radius R is related to the dimensionless radius ρ by

$$R = \rho\sqrt{\frac{\Sigma_0}{4\pi}}, \qquad \text{[II.1.6]}$$

where Σ_0 (=60 Å^2) is the surface area per head group of the surfactant (3).

Finally, by denoting the overall surfactant (water) mole fraction as X_s (X_w), the mass conservation law for both surfactant and water molecules can be simply expressed in terms of the second and the third moment of ρ,

$$X_s = e^{-\xi+\beta\Delta\mu_s} + \langle \rho^2 \rangle x_d, \qquad \text{[II.1.7]}$$

$$X_w = e^{-\eta+\beta\Delta\mu_w} + \lambda\langle \rho^3 \rangle x_d, \qquad \text{[II.1.8]}$$

where x_d is the droplet mole fraction which is defined as

$$x_d = \int_{\rho_l}^{\infty} d\rho f(\rho). \qquad \text{[II.1.9]}$$

Here the lower integration limit, ρ_l, corresponding to the smallest aggregates, should be $\sqrt{2}$. As it stands, the first terms on the right hand side of Eq. [II.1.7] and [II.1.8] are originated from monomers, whereas the second terms are contributions from the droplets.

Equations [II.1.1]–[II.1.9] complete the description of the three-component micromulsion in terms of its physical parameters, and they can also be used to determine the phase boundaries for a given system. To calculate the distribution function, $f(\rho)$, we need first to evaluate the two Lagrangian multipliers ξ and η using Eq. [II.1.7] and [II.1.8] for given X_s and X_w. Once ξ and η are determined the distribution function itself is uniquely defined. It is interesting to note that the distribution function $f(\rho)$ has very different asymptotic behaviors in the single-phase and in the two-phase regions because of different thermodynamic constraints. In the single-phase region, since both ξ and η are nonzero, the large droplets are inhibited by the energy cost ($\sim\eta\rho^3$) of water cores of the droplets, therefore $f(\rho)$ decays as $\sim e^{-\eta\rho^3}$ for $\rho \to \infty$. On the other hand, in the two-phase region, since ξ is nonzero but η is zero, the existence of large droplets is only inhibited by the surface energy cost ($\sim\xi\rho^2$) of the surfactants on the interfaces, therefore $f(\rho)$ decays as $\sim e^{-\xi\rho^2}$ for $\rho \to \infty$.

In the rest of the paper we will focus on the two-phase region and seek an analytic solution in this region using the theory outlined above. In the two-phase region, water molecules inside the droplets can exchange freely with the water reservoir, hence we have $\eta = 0$. By relaxing this thermodynamic constraint the solution of Eqs. [II.1.7] and [II.1.8] is greatly simplified, because these two equations become decoupled and ξ can be solved from Eq. [II.1.7] alone. Physically it means that the distribution function is uneffected by the amount of water present in the reservior. We notice that in this thermodynamic region the distribution function, $f(\rho)$, is peaked at

$$\rho_{max} \simeq \rho_s \frac{8\pi\beta\kappa}{\xi\rho_s^2 + 8\pi\beta\kappa}, \qquad \text{[II.1.10]}$$

and has a half width

$$\sigma \simeq \frac{\rho_s}{\sqrt{2(\xi\rho_s^2 + 8\pi\beta\kappa)}}. \qquad \text{[II.1.11]}$$

For $8\pi\beta\kappa \gg \xi\rho_s^2$, we have (14) $\rho_{max}/\sigma \simeq \sqrt{16\pi\beta\kappa} \gg 1$. This allows us to further simplify Eqs. [II.1.5] and [II.1.9] by extending the lower integration limit from a finite value, ρ_l, to the minus infinity. Such an approximation

sacrifices little numerical accuracy since the integrand decays exponentially fast for $\rho \ll \rho_1$, (see III.3 for more discussions). Therefore we can write $\langle \rho^n \rangle x_d$ in an analytical form,

$$\langle \rho^n \rangle x_d = (n+1)!\sqrt{2\pi y} \times \exp\left[\beta\Delta\mu_d - 8\pi\beta\kappa + \frac{1}{2y}\right] \times \left(\frac{\rho_s}{16\pi\beta\kappa y}\right)^{n+2} G_{n+1}(y), \quad [II.1.12]$$

where y and $G_n(y)$ are given by

$$y = \frac{\xi\rho_s^2 + 8\pi\beta\kappa}{2(8\pi\beta\kappa)^2}, \quad [II.1.13]$$

and

$$G_n(y) = \sum_{k=0}^{E(n/2)} \frac{1}{(n-2k)!(k)!}\left(\frac{y}{2}\right)^k, \quad [II.1.14]$$

respectively. Since $\langle \rho^0 \rangle = 1$, from Eq. [II.1.12] we obtain the mole fraction of droplets x_d as

$$x_d = \frac{\rho_s^2}{(16\pi\beta\kappa y)^2}\sqrt{2\pi y} \times \exp\left[\beta\Delta\mu_d - 8\pi\beta\kappa + \frac{1}{2y}\right]. \quad [II.1.15]$$

Using Eqs. [II.1.12], [II.1.14], and [II.1.15] we can write the first three moments of ρ in a parametric form:

$$\langle \rho \rangle = \frac{\rho_s}{16\pi\beta\kappa}\frac{1+y}{y}, \quad [II.1.16]$$

$$\langle \rho^2 \rangle = \frac{\rho_s^2}{(16\pi\beta\kappa)^2}\frac{1+3y}{y^2}, \quad [II.1.17]$$

and

$$\langle \rho^3 \rangle = \frac{\rho_s^3}{(16\pi\beta\kappa)^3}\frac{1+6y+3y^2}{y^3}. \quad [II.1.18]$$

Finally the variance of the distribution ϵ, which is the square of the polydispersity of the droplets, can be written as

$$\epsilon \equiv \frac{\langle \rho^2 \rangle}{\langle \rho \rangle^2} - 1 = y\frac{1-y}{(1+y)^2}. \quad [II.1.19]$$

This last equation can also be expressed in term of $\langle \rho \rangle$ by eliminating y using Eq. [II.1.16]. The final result is

$$\epsilon = \frac{1}{16\pi\beta\kappa}\frac{\rho_s}{\langle \rho \rangle}(1 - O(\epsilon^2)). \quad [II.1.20]$$

The above equation should be compared with that for a single-phase microemulsion. Safran (15) and Borkovec *et al.* (1) have calculated the variance ϵ when the total surfactant mole fraction is relatively high so that the surfactant monomer concentration can be neglected. Their result is

$$\epsilon = \frac{1}{48\pi\beta\kappa\left(1 - \frac{2}{3}\frac{\rho_0}{\rho_s}\right)} \times (1 + O(\epsilon^2)), \quad [II.1.21]$$

where ρ_0 is the Schulmans radius which is related to the mean droplet radius by $\langle \rho \rangle = \rho_0[1 - 2\epsilon + O(\epsilon^2)]$ (1). For a system with a stiff surfactant layer $48\beta\kappa \gg 1$, $\langle \rho \rangle = \rho_0$.

It should be pointed out that for a single-phase microemulsion the system consists, intrinsically, of two length scales ρ_0 and ρ_s, whereas for a two-phase microemulsion the system has only one length scale ρ_s. This makes the two-phase region particularly useful for measuring the spontaneous radius, ρ_s, for a given system. Physically the spontaneous radius ρ_s characterizes the natural bending curvature of surfactant molecules, and to a large extent ρ_s only depends on the surfactant molecular shape and the solvent condition. The Schulmans radius, ρ_0, on the other hand, characterizes the ultimate size of the droplets at high volume fraction (1) and depends solely on the water to surfactant molar ratio, ω. It should also be pointed out that in the limit of very small polydispersity $\epsilon \to 0$, i.e., when κ is very large, the mean droplet radius $\langle \rho \rangle$ approaches two different limiting values in the different phases. In the single-phase region $\langle \rho \rangle \to \rho_0$ and in the two-phase region $\langle \rho \rangle \to \rho_s$. Therefore in the limit of small polydispersity we can replace ρ_0 by $\langle \rho \rangle$ in Eq. [II.1.21] and write ϵ as

$$\epsilon \simeq \frac{1}{48\pi\beta\kappa\left(1 - \frac{2}{3}\frac{\langle \rho \rangle}{\rho_s}\right)} \times (1 + O(\epsilon^2)). \quad [II.1.22]$$

Because the polydispersity is a continuous function of the droplet size, Eqs. [II.1.20] and [II.1.22] should be equal at the phase boundary, and hence we find the emulsification failure condition $\langle \rho \rangle = \rho_s$. This phase stability limit for the small polydispersity is consistent with that obtained by Safran and Turkevich (16) using a different approach.

II.2 SANS from a Distribution of Polydispersed Spherical Shells

To test the above theoretical calculations we have used the small-angle neutron scattering technique to determine the mean radius of droplets, $\langle R \rangle = \langle \rho \rangle\sqrt{\Sigma_0/4\pi}$, and the polydispersity, $\sqrt{\epsilon}$, at different droplet concentrations. The structural information of the droplets in real space can be obtained by deconvoluting the measured neutron scattering intensity $I(Q)$ based on certain reliable scattering models.

First, let us consider the neutron scattering intensity, $I(Q)$, from a set of identical particles; this is given by

$$I(Q) = N_p P(Q) S(Q), \quad [II.2.1]$$

where N_p is the number density of the scattering particles, $P(Q)$ is the particle form factor, and $S(Q)$ is the structure factor. Unlike an aqueous solution, the interaction between the droplets in a water-in-oil microemulsion is mainly due to a hard-core repulsion. For the hard-sphere interaction we found, using the Percus–Yevick approximation (17), that the first maximum in $S(Q)$ is about 1.01 for the highest concentration ($\phi = 2\%$) used in the experiment. This suggests that the interaction between the droplets is negligible and the scattering intensity is dominated by the form factor $P(Q)$. For a spherical shell with the inner radius R_i and the outer radius R_o, the form factor $P(Q)$ can be calculated using a linear superposition of scattering amplitudes $F(QR_i)$ and $F(QR_o)$ of solid spheres with radius R_i and R_o, respectively. This gives

$$P(Q) = [F(QR_o) - F(QR_i)]^2, \quad [II.2.2]$$

where

$$F(QR_j) = \frac{4\pi R_j^3}{3}(\bar{\rho}_j - \bar{\rho}_s) \times \frac{\sin(QR_j) - QR_j\cos(QR_j)}{(QR_j)^3}, \quad [II.2.3]$$

where j stands for either i (inner) or o (outer radius). In Eq. [II.2.3], $\bar{\rho}_j$ and $\bar{\rho}_s$ are the neutron scattering length densities of the sphere and the solvent, respectively.

Next, we consider the scattering from a distribution of particles with different sizes. We assume the size of the scattering particle can be characterized by a distribution function $f(R)$. In this case we can differentiate Eq. [II.2.1] and write $dN_p = N_p f(R)dR$, where dN_p/N_p represents the fraction of droplets with the radii in the interval between R and $R + dR$. Integrating over the scatterings from particles of all sizes we obtain the total scattering intensity:

$$I(Q) = N_p \int_0^\infty P(Q) f(R) dR. \quad [II.2.4]$$

For simplicity, hereafter, we use the Schultz distribution function $f_s(R)$ to model the size distribution of AOT microemulsion droplets (3). Such an approximation has been used previously, and has been shown to be consistent with various analysis procedures, such as inverse Laplace transformation and histogram method, for neutron scattering and light scattering data (2, 3). Simple form of Schultz distribution function also allows an analytic calculation of the scattering intensity for various shapes of scattering entities. For spherical scattering objects the Schultz distribution function is given by

$$f_s(R) = \frac{(z+1)^{z+1}}{\langle R\rangle \Gamma(z+1)} \left(\frac{R}{\langle R\rangle}\right)^z \times \exp\left[-(z+1)\frac{R}{\langle R\rangle}\right], \quad [II.2.5]$$

where $\langle R\rangle$ is the mean droplet size and z is related to the polydispersity by $\epsilon = 1/(z+1)$. The final expression for the total scattering intensity, $I(Q)$, is given in the Appendix (18).

III. EXPERIMENTAL

III.1 Sample Preparation

The surfactant, sodium di-2-ethylhexylsulfosaccinate, was purchased from Fluka Chemical Company. The surfactant was treated with the activated charcoal and then twice recrystallized from methanol. It was stored in the vacuum before usage. Our previous measurements indicated that with such a purification process the experimental results were reproducible within each batch, and variations could occur among different batches.

We have used deuterated water, D_2O (19), as the internal phase of the microemulsion and used deuterated decane (19), $C_{10}D_{22}$, as the solvant. The scattering length densities of D_2O ($\bar{\rho}_{D_2O} = 6.33 \times 10^{-6}$ Å^{-2}) and $C_{10}D_{22}$ ($\bar{\rho}_{C_{10}D_{22}} = 6.36 \times 10^{-6}$ Å^{-2}) are closely matched and they are very different from the scattering density of the surfactant tail, which consists mainly of hydrocarbons, ($\bar{\rho}_{tail} = -0.49 \times 10^{-6}$ Å^{-2}). Therefore the scattering entities in the sample are spherical shells with only the surfactant "tails" being visible to the neutrons. As mentioned in our earlier publication (5), such a scattering sample is superior to a sample consisting of solid-spheres with normal water, H_2O, as the internal phase of the microemulsion. This is because the spherical-shell sample has a very low hydrogen incoherent scattering and the coherent scattering intensity as a function of the scattering wavenumber exhibits a sharp minimum, which entailed a tight fit for both the mean radius and the polydispersity of the droplets.

All the scattering samples, with the dispersed-phase (D_2O + AOT) volume fraction of ϕ = 2, 1, 0.5, 0.2, 0.1, and 0.05%, have the fixed water to surfactant molar ratio of $\omega \simeq 30$. This was achieved by successively diluting a master solution of ϕ = 2%. To convert the volume fraction ϕ to the surfactant mole fraction X_s, we use the equation (20)

$$X_s = \frac{A\phi}{B\phi + C(1-\phi)}, \quad [III.1.1]$$

where A = 194.9 cm^3/mol, B = 6042.4 cm^3/mol, and C = 936.6 cm^3/mol.

III.2 Small-Angle Neutron Scattering Measurements

The small-angle neutron scattering experiment was performed on a high resolution spectrometer of the High Flux Beam Reactor at Brookhaven National Laboratory. The incident neutron wavelength, Λ, was 5.3 ± 0.3 Å. We successively used a set of collimating pinholes of diameters 10, 8, and 6 mm, with the 6-mm pinhole being closest to the sample. The distance between the sample and the detector was 1800 mm, which gives a usable Q-range of 0.01 Å$^{-1} \leqslant Q \leqslant$ 0.2 Å^{-1}. Here the magnitude of the scattering wave-vector Q is related to the scattering angle θ by $Q = (4\pi/\Lambda)\sin(\theta/2)$. The neutron scattering intensity was measured by a two-dimensional detector, and a circular integration over the scattering intensity at the fixed scattering angle was performed to give better statistics. We subtracted out the background scatterings due to quartz windows and the solvent. The incoherent scattering from hydrogens in AOT molecules was also subtracted out. Further precaution was taken to eliminate inhomogeneities in the detector's sensitivities at different pixels by normalizing all the scattering intensities with that from a 1-mm water sample. Therefore our scattering data are given in the absolute units of water scattering intensity.

III.3 Experimental Results and Data Analysis

Three set of the SANS data measured at ϕ = 2, 0.5, and 0.1% are shown in Fig. 2. Two distinct features must be emphasized: first, all the data contain a minimum, which is a characteristic of the scattering from the spherical shells. The location of this minimum moves to larger Q as the solution is diluted. This indicates that the size of the droplets is decreased at lower surfactant concentration. Secondly, the scattering intensity peak at $q \to 0$ becomes broader and the second scattering peak becomes less pronounced at lower surfactant concentrations. This suggests an increase in the polydispersity as the sample is diluted. Using a non-linear least-squares fitting routine (21), we obtained good fits to the spherical shell-model (Eqs. [II.2.2]–[II.2.5]), and they are shown by the solid lines in the figure. The thickness of the shell determined by the sample with ϕ = 2% is ~8 Å, which is close to our earlier measurement (5). This thickness was kept fixed for the fittings to the rest of concentrations.

For the sample with the lowest surfactant concentration, i.e. ϕ = 0.05%, the scattering intensity decreases dramatically and the data (not shown) is essentially flat on the scale of Fig. 2. This suggests that there is no aggregation at this concentration and the scattering is from the surfactant monomers only. From this observation we conclude that the CMC value is in the range 0.05% $\leqslant \phi \leqslant$ 0.1% (or $1.04 \times 10^{-4} \leqslant X_s \leqslant 2.07 \times 10^{-4}$).

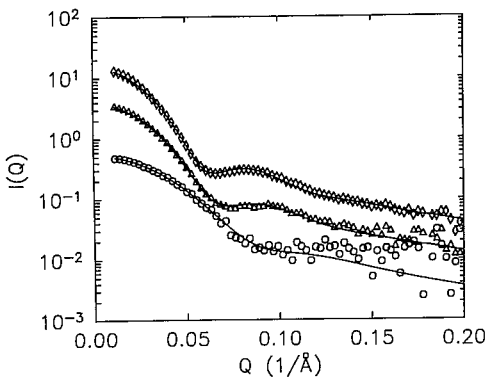

FIG. 2. The neutron scattering intensity $I(Q)$ vs. wavenumber Q. Scattering intensities are measured at the following dispersed-phase volume fractions ϕ (or surfactant concentrations X_s): 2% (3.75×10^{-3}), 0.5% (1.01×10^{-3}), and 0.1% (2.07×10^{-4}). They are indicated by diamonds, triangles, and circles, respectively. The solid curves are obtained by the non-linear least-squares fit using Eqs. [II.2.4] and [II.2.5].

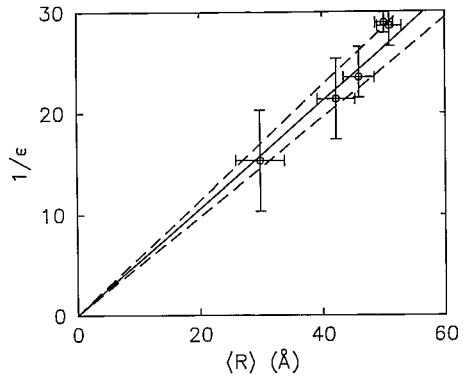

FIG. 3. The Inverse of the variance $1/\epsilon$ vs. the mean droplet size $\langle R\rangle$. The circles are obtained from the SANS data. The size of error bars is equal to two standard deviations determined by the non-linear fitting routine (21). As shown in the figure, the data can be described reasonably well by Eq. [II.1.20]. A linear fit to the data, as shown by the solid line, gives a value of 0.53 ± 0.04 Å^{-1} for the slope of the straight line. The two dash lines indicate the uncertainties in determining this slope.

The mean droplet radius, $\langle R\rangle$, and the polydispersity, $\sqrt{\epsilon}$, extracted from the above fitting can be used to check the theoretical prediction of Eq. [II.1.20]. In Fig. 3 we plot $1/\epsilon$ vs. $\langle R\rangle$, where we expect a linear curve with a slope of $16\pi\beta\kappa/R_s$ and an intercept of zero. Our experimental data can be fit reasonably well to a straight line with the slope of 0.53 Å^{-1}. The two dash lines in the figure indicate the errors, ±0.04 Å^{-1}, of the slope. From the measured slope, if either value of the elastic constant, κ, or the spontaneous radius, R_s is known, the other value can be deduced.

In Fig. 4 we plot, for various surfactant concentration X_s, the mean droplet radius, $\langle R\rangle$, and the polydispersity, $\sqrt{\epsilon}$, simultaneously. We find that the microemulsion droplet size de-

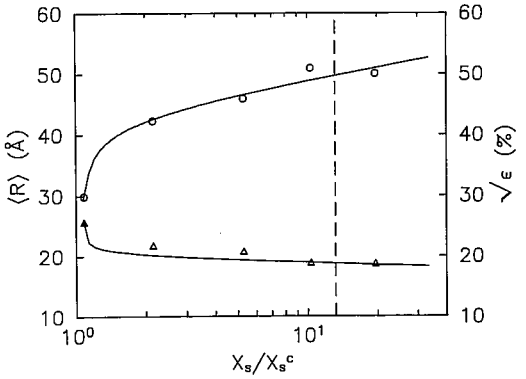

FIG. 4. The mean radius $\langle R \rangle$ (circles) and the polydispersity $\sqrt{\epsilon}$ (triangles) vs. the reduced surfactant concentration X_s/X_s^c. The vertical dash line indicates the calculated emulsification failure boundary. As shown in the figure, in the two-phase region the microemulsion droplet size decreases and the polydispersity increases as the CMC is approached, i.e., when $X_s/X_s^c \to 1$. In the single-phase region both the droplet size and the polydispersity remain constant. The solid curves are the theoretical fits which show good agreements with the measurements.

creases while its polydispersity increases when the surfactant concentration is decreased below $X_s \leqslant 2.0 \times 10^{-3}$ ($X_s/X_s^c \leqslant 10$ or $\phi \leqslant 1\%$). Above this concentration both $\langle R \rangle$ and $\sqrt{\epsilon}$ remain approximately constant. To compare these results to the theoretical calculations in Eqs. [II.1.16] and [II.1.19], one has to determine the value of the Lagrangian multiplier ξ using Eq. [II.1.7]. Before solving this equation we have to fix as many physical parameters as possible from previous measurements. These include the surface area per AOT surfactant head group (3) $\Sigma_0 = 60$ Å^2, the specific volume of water molecule $v_w = 30.3$ Å^3, and the chemical potential of water molecule $\beta\Delta\mu_w = -8$, which was measured by the solubility of water in isooctane (22). It should be pointed out that while $\beta\Delta\mu_w$ is an important parameter in determining the phase boundary of the microemulsion, it is an irrelavent parameters for computing the droplet size distribution function in the two-phase region because $\eta = 0$. For fixed ratio of $\beta\kappa/R_s$, determined by the slope in Fig. 3, we are left with only three fitting parameters, $\beta\kappa$, $\beta\Delta\mu_s$, and $\beta\Delta\mu_d$. Since our SANS experiment gives measurements for $\langle R \rangle$ and ϵ as a function of X_s, we can self-consistently determine all these parameters.

As shown by the solid curves in Fig. 4, our experimental data can be well fitted to the theory using the following set of parameters: $\beta\kappa = 0.6 \pm 0.1$, $\beta\Delta\mu_s = -8.5 \pm 0.1$, and $\beta\Delta\mu_d = -17 \pm 3$. Since we already knew the ratio $16\pi\beta\kappa/R_s = 0.53$ from Fig. 3, we obtain the spontaneous radius for our system to be $R_s = 57 \pm 14$ Å. By the definition of CMC (1), $X_s^c \exp(-\beta\Delta\mu_s) = 1$, we obtain $X_s^c = 2.0 \times 10^{-4}$ for our system. Using $\omega = 30$ and the parameters obtained above, we are able to determine the phase boundary, X_s^u, between the single-phase and the two-phase region by Eqs. [II.1.5] and [II.1.7]. This gives $X_s^u \simeq 2.4 \times 10^{-3}$, which is shown by a vertical dash line in Fig. 4. This calculation is consistant with the observation that above $X_s \simeq 2 \times 10^{-3}$, ($\phi = 1\%$), the mean droplet radius and the polydispersity remain constant as expected for a single-phase microemulsion.

We also examine the mole fraction x_d of the droplets as a function of X_s. Here x_d is proportional to the total number, N_p, of scattering droplets in the scattering volume, i.e., $x_d = CN_p$. Using the calculated x_d at different surfactant concentrations and N_p obtained from the measured scattering intensity, we find the proportional constant $C \simeq 8 \times 10^{-14}$. In Fig. 5 we plot both the measured and the calculated x_d as a function of X_s/X_s^c. We find that the mole fraction of droplets x_d decreases dramatically as the surfactant concentration decreases, and vanishes as the CMC is approached ($X_s/X_s^c \to 1$). As it can be seen in Fig. 5, our measurement is consistent with the theory except at the highest surfactant concentration ($\phi = 2\%$), where the deviation is expected because the microemulsion is already in the single-phase region in which our calculation is not applicable.

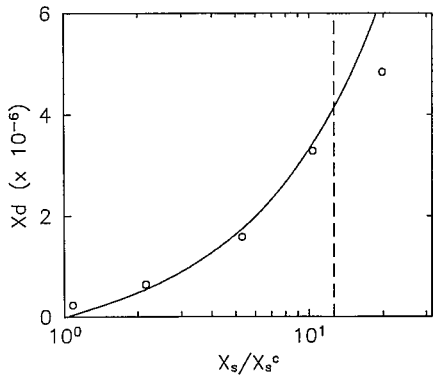

FIG. 5. The mole fraction of droplets x_d vs. the reduced surfactant concentration X_s/X_s^c. The mole fraction of droplets x_d decreases as the reduced surfactant concentrations X_s/X_s^c decreases. The droplets disappear at $X_s/X_s^c = 1$. The solid curve is a theoretical calculation based on Eq. [II.1.15]. Large deviation at the highest surfactant concentration, ($X_s/X_s^c \geqslant 12$, or $\phi > 1\%$), is expected because the system is already in the single-phase region. The vertical dash line indicates the calculated emulsification failure boundary.

Finally, we compare the Schultz distribution function with the statistical model at volume fractions $\phi = 0.1$ and 1%. These concentrations represent the two extremes in the two-phase region as shown in Fig. 4. For $\phi = 0.1\%$ the system is close to the CMC; the microemulsion droplets attain the minimum size ($\langle R \rangle \simeq 30$ Å) and the maximum polydispersity ($\sqrt{\epsilon} \simeq 26\%$). For $\phi = 1\%$ the system is close to the single-phase region; the microemulsion droplets attain the maximum size ($\langle R \rangle \simeq 50$ Å) and the minimum polydispersity ($\sqrt{\epsilon} \simeq 19\%$). In Fig. 6 we plot the Schultz (dash–dot curves) and the statistical (solid curves) distribution functions together for the two concentrations. We find that even though these two distribution functions have the same mean and variance, the peak positions are slightly different (the difference is ~4 Å at $\phi = 0.1\%$ and ~1 Å at $\phi = 1\%$), with the Schultz distribution being consistently lower than the statistical one. This is because the Schultz distribution function has a slower fall-off at large radius. Overall, however, the Schultz distribution function mimics the statistical model reasonably well. From Fig. 6 we also find that dilution shifts the peak position of the distribution functions toward smaller values of R, while the width of the distribution functions is almost constant. Therefore the apparent increase of the polydispersity at the lower concentration is mainly due to the decrease of the microemulsion droplet size. Note that even at the lowest surfactant concentration, the statistical distribution still decays very fast toward the small droplet radius, which justifies the approximation we made earlier for obtaining Eq. [II.1.5] by extending the lower integration limit to minus infinity.

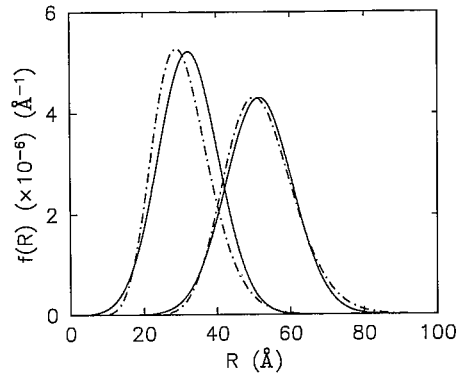

FIG. 6. The size distribution function $f(R)$ vs. the droplet radius R. The solid curves show the statistical distribution and the dash–dot curves show the Schultz distribution function. The dispersed-phase volume fraction ϕ (or the surfactant concentrations X_s) is 0.1% (2.07×10^{-4}) for the two left curves and 1% (1.97×10^{-3}) for the two right curves.

In passing, we want to mention that a simpler derivation for the mean droplet radius, $\langle R \rangle$, as a function of the dispersed-phase volume fraction, ϕ, was given by Safran recently (23). Assuming zero solubility of water in oil, Safran found (24)

$$\frac{\langle R \rangle}{R_s} = 1 + \frac{\log\left[\frac{v_w}{v}(\phi - \phi_0)\right]}{8\pi\beta\kappa}, \quad \text{[III.3.1]}$$

where $v\,(=4\pi\langle R \rangle^3/3)$ is the mean volume of the droplets and ϕ_0 is the volume fraction at the CMC. Using $v_w = 30.3$ Å^3 and Eq. [III.1.1], we obtain $\phi_0 = 0.065\%$. By fitting the measured $\langle R \rangle$ with Eq. [III.3.1] (see Fig. 7), we find $\beta\kappa \simeq 1$ and $R_s \simeq 92$ Å. Considering the simplicity of Safran's theory, the obtained numerical values for $\beta\kappa$ and R_s are still rea-

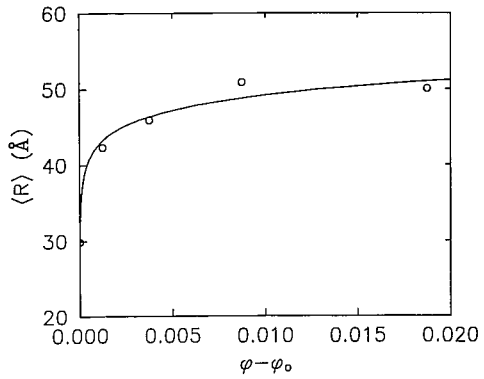

FIG. 7. The mean droplet radius $\langle R \rangle$ vs. the dispersed-phase volume fraction, $\phi - \phi_0$. Here ϕ_0 is the volume fraction at the CMC. Circles are experimental data, and the solid curve is the fit to Eq. [III.3.1].

sonable. However, we expect the calculation to be less reliable for systems with higher CMC values.

III.4 Discussions

It is interesting to note that the elastic bending energy obtained from our scattering measurement ($\beta\kappa \simeq 0.6$) is approximately six times smaller than that measured by the neutron spin-echo (NSE) technique (10, 25). Safran (11) pointed out recently that the large difference in κ can be reconciled if the saddle-splay energy $\bar{\kappa}$ of the microemulsion droplets is taken into account explicitly. Without loss of generality, we write the elastic free energy, F_{bend}, for the microemulsion droplets as

$$F_{\text{bend}} = \frac{\kappa}{2}\int (C_1 + C_2 - 2/R_s)^2 dS + \bar{\kappa}\int C_1 C_2 dS, \quad \text{[III.4.1]}$$

where C_1 and C_2 are the principal radii of curvatures and the integration is over the entire surface of the droplet. The Gauss–Bonnet theorem implies that the saddle-splay contribution is a topological constant and in the case of uniform-sized spherical droplets it gives $4\pi\bar{\kappa}n$, where n is the number of droplets. However, with the constant-surface and constant-volume conditions, varying the polydispersity varies the number of droplets; consequently the $\bar{\kappa}$ term in Eq. [III.4.1] cannot be neglected. Furthermore, we know that for a spherical microemulsion to be thermodynamically stable $\bar{\kappa}$ has to be negative. Statically, a negative $\bar{\kappa}$ tends to favor a larger number of droplets and hence increases the polydisperisty (25). Dynamically, on the other hand, a negative $\bar{\kappa}$ means that the bending of a spherical surfactant film against its natural curvature (i.e., making the droplet surface rippled) will be energetically costly. Consequently, the droplet shape fluctuations are greatly inhibited. The enhancement of the equilibrium polydispersity and the suppression of the shape fluctuations make the effective elastic bending energy obtained from the static measurements smaller than its bared value (see Eq. [II.1.20]) and NSE measurement. Safran (11) has calculated the effective elastic bending energy, κ', and the effective spontaneous radius, R_s', by taking into account the saddle-spray elastic energy $\bar{\kappa}$. For spherical droplets since $C_1 = C_2 = 1/R$, Eq. [III.4.1] is simplified and we obtain

$$F_{\text{bend}} = \frac{\kappa'}{2}\int (2/R - 2/R_s')^2 dS + \text{Const}, \quad \text{[III.4.2]}$$

where

$$\kappa' = \kappa\left(1 + \frac{\bar{\kappa}}{2\kappa}\right), \quad \text{[III.4.3]}$$

$$R_s' = R_s\left(1 + \frac{\bar{\kappa}}{2\kappa}\right). \quad \text{[III.4.4]}$$

Because the SANS technique measures predominantly the static component of the fluctuations (26), our measured elastic bending constant, κ, and the spontaneous radius, R_s, should be identified as κ' and R_s', respectively, and they are smaller than the bared values. Combining the static (SANS) and the dynamic (NSE) measurements we find $\bar{\kappa} \simeq -1.7\kappa$ which is consistent with Ref. (25).

Finally, we want to point out that because the statistical model involves many parameters, it is impossible to determine all of them

in one experiment. Our strategy in the interpretation of the experimental data is to use the minimum number of those parameters which have the most physical significance while keeping the others fixed. The fixed parameters include the geometrical constants for the surfactant, Σ_0, and water, v_w, molecules and the chemical potential of water in oil, $\Delta\mu_w$. The numerical value for these parameters were determined in previous experiments and are expected to be valid for the present experiment. The most uncertainty in our calculation is the assumption that $\nu = 1$. According to the literature (1), ν can have a range of values depending on theoretical models. However, by setting $\nu = 2$ and following the same calculation we found that our main results are not affected significantly. In this case both $\beta\kappa$ and R_s only increase by ~3%, which is less than the uncertainties in the data itself. This calculation demonstrates the internal consistency of the theory and suggests that the true value of ν may be close to what we have used. In fact, by combining the theoretical analyses of Lothe–Pound (27, 28) for the entropy of mixing and of Helfrich (29) for the thermal fluctuations of droplet interfaces we find $\nu = 2.2$, in agreement with our expectation.

IV. CONCLUSIONS

We have performed small-angle neutron scattering experiments for a very dilute water-in-oil AOT microemulsion. At the fixed water-to-surfactant molar ratio of $\omega = 30$, we observed a decrease in the microemulsion droplet radius and an increase in the polydispersity when the dispersed-phase volume fraction was diluted to less than 1%. This interesting phase behavior was investigated in terms of emulsification failure process. In doing so, we have derived an analytic solution for a three-component microemulsion in the two-phase region based on the theory of Borkovec *et al.* (1). This solution allows us to make a connection between the thermodynamic phase behaviors and various physical parameters. Among them the elastic bending energy, κ, the spontaneous radius, R_s, and the critical micellar concentration, X_s^c, are of great theoretical and practical interests. Our calculations show that in the two-phase region the microemulsion droplet size is governed by a single length scale, namely the spontaneous radius R_s. While in the single-phase region there are two relevant length scales, namely the spontaneous radius R_s and the Schulman radius R_0. This unique feature of the two-phase microemulsion allows us to make a quantitative measurement of the spontaneous radius R_s, which we found to be $R_s = 57 \pm 14$ Å for AOT microemulsion. Our calculations also show that near the critical micellar concentration (CMC) all the physical parameters, such as the mean droplet radius, the polydispersity, and the number density of the microemulsion droplets, are extremely sensitive to the surfactant concentration. This entails a reliable measurement of the CMC value for the microemulsion. Experimentally we found $X_s^c = 2.0 \times 10^{-4}$. The CMC value determined by the SANS measurement compares favorably to that of AOT in variety of hydrocarbon solvents (30). Finally, we find that the effective elastic bending energy for this AOT microemulsion is $\kappa\beta \simeq 0.6$. A plausible mechanism is proposed which explains the large difference in the elastic bending energy, κ, measured statically and dynamically.

APPENDIX

The neutron scattering intensity distribution $I(Q)$ from a dilute polydispersed sample is given by

$$I(Q) = N_p \int_0^\infty P(Q) f(R) dR, \quad \text{[A.1]}$$

where N_p is the number density of the scattering particles, $P(Q)$ is the particle form factor, and $f(R)$ is the particle size distribution function. For a concentric spherical shell with an inner radius R_i and an outer radius R_o, $P(Q)$ can be written as

$$P(Q) = [F(QR_o) - F(QR_i)]^2, \quad \text{[A.2]}$$

where

$$F(QR_j) = \frac{4\pi R_j^3}{3}(\bar{\rho}_j - \bar{\rho}_s) \times \frac{\sin(QR_j) - QR_j\cos(QR_j)}{(QR_j)^3}. \quad [A.3]$$

Here $\bar{\rho}_j$ and $\bar{\rho}_s$ are the neutron scattering length densities of the sphere and the solvent, respectively. For a spherical-shell sample the matching condition for the scattering length densities is given by $\bar{\rho}_i = \bar{\rho}_s \neq \bar{\rho}_o$. Using the Schultz distribution function,

$$f_s(R) = \frac{(z+1)^{z+1}}{\langle R\rangle\Gamma(z+1)}\left(\frac{R}{\langle R\rangle}\right)^z \times \exp\left[-(z+1)\frac{R}{\langle R\rangle}\right], \quad [A.4]$$

the scattering intensity distribution $I(Q)$ in Eq. [A.1] has the following form (18):

$$I(Q) = (\rho_0 - \rho_s)^2 v^2[p^6 t_2(QR_i) + t_2(QR_o) - 2t_3(QR_0, p)]. \quad [A.5]$$

Here $v(=4\pi R_0^3/3)$ is the volume of the droplet, $p(=R_i/R_o)$ is a thickness parameter, and t_2 and t_3 are functions which are defined as

$$t_2(y) = \frac{9}{2(z+1)y^6} \times \left\{(z+1)\left[1 - \frac{\cos((z+1)w)}{(1+4u^2)^{(z+1)/2}} - \frac{2y\sin((z+2)w)}{(1+4u^2)^{(z+2)/2}}\right] + y^2(z+2) \times \left[1 + \frac{\cos((z+3)w)}{(1+4u^2)^{(z+3)/2}}\right]\right\}, \quad [A.6]$$

and

$$t_3(y,p) = \frac{9}{2(z+1)y^6}\left\{(z+1) \times \left[\frac{\cos((z+1)v_-)}{(1+u_-^2)^{(z+1)/2}} - \frac{\cos((z+1)v_+)}{(1+u_+^2)^{(z+1)/2}}\right] + (z+1)\left[\frac{y_-\sin((z+1)v_-)}{(1+u_-^2)^{(z+1)/2}} - \frac{y_+\sin((z+1)v_+)}{(1+u_+^2)^{(z+1)/2}}\right] + y^2p(z+2)\left[\frac{\cos((z+3)v_-)}{(1+u_-^2)^{(z+3)/2}} + \frac{\cos((z+3)v_+)}{(1+u_+^2)^{(z+3)/2}}\right]\right\}. \quad [A.7]$$

In the above, the new variables are $y_\pm = (1 \pm p)y$, $u = y/(z+1)$, $w = \arctan(2u)$, $u_\pm = (1 \pm p)y/(z+1)$, and $v_\pm = \arctan(u_\pm)$.

ACKNOWLEDGMENTS

We thank Dr. D. Schneider for his technical assistance and Mr. J. Sung for the preparation of the scattering samples. We also appreciate helpful discussions with Drs. S. A. Safran and S. T. Milner during the preparation of this manuscript.

REFERENCES

1. Borkovec, M., Eicke, H. F., and Ricka, J., *J. Colloid Interface Sci.* **131,** 366 (1989).
2. Chen, S. H., Lin, T. L., and Huang, J. S., *in* "Physics of Complex and Supermolecular Fluids" (S. A. Safran and N. A. Clark, Eds), p. 285. John Wiley & Sons, New York, 1987.
3. Kotlarchyk, M. Stephens, R. B., and Huang, J. S., *J. Phys. Chem.* **92,** 1533 (1988).
4. Kotlarchyk, M., Chen, S. H., Huang, J. S., and Kim, M. W., *Phys. Rev. A* **29,** 2054 (1984).
5. Huang, J. S., Sung, J., and Wu, X-L., *J. Colloid Interface. Sci.* **132,** 34 (1989).
6. Chen, S. H., and Huang, J. S., *Phys. Rev. Lett.* **18,** 1888 (1985).
7. Huang, J. S., and Kotlarchyk, M., *Phys. Rev. Lett.* **57,** 2587 (1986).
8. Sheu, E. Y., Chen, S. H., Huang, J. S., and Sung, J. C., *Phys. Rev. A* **39,** 5867 (1989).
9. As we shall see later in the text, this effective elastic bending energy is the splay elastic bending energy κ renormalized by the saddle-splay elastic energy $\bar{\kappa}$.
10. Huang, J. S., Milner, S. T., Farago, B., and Richter, D., *Phys. Rev. Lett.* **59,** 2600 (1987).
11. Safran, S. A., submitted for publication.
12. By definition $\lambda = \sqrt{\Sigma_o^3/36\pi v_w^2}$. Here we have used commonly accepted values for the specific volume of water, $v_w = 30.3$ Å^3, and the surface area per AOT surfactant, $\Sigma_o = 60$ Å^2.
13. The exponent is given by $\nu = 3(1-\tau) + 2\alpha$, where τ comes from the entropy of mixing and α is from renormalization of the elastic bending energy, κ, due the thermal undulation. Depending on different models, ν can have very different values. Since the strongest ρ-dependence is in the exponential part of the distribution function, we simply set $\nu = 1$.
14. It can be shown numerically that for the parameters used in the experiment ξ is a monotonical function of X_s and $(\xi\rho_s^2)_{max} \sim O(1)$. Therefore, the condition $8\pi\beta\kappa \gg \xi\rho_s^2$ always holds.
15. Safran, S. A., *J. Chem. Phys.* **87,** 2073 1983.
16. Safran, S. A., and Turkevich, L. A., *Phys. Rev. Lett.* **50,** 1930 (1983).
17. Hess, W., and Klein, R., *Adv. Phys.* **32,** 173 (1983).
18. Hayter, J. B., *in* "Physics of Amphiphiles: Micelles, Vesicles and Microemulsions" (V. Degiorgio and M. Corti, Eds.), p. 864. North-Holland, Amsterdam, 1985.
19. The chemicals were purchased from Cambridge Isotopes Inc.
20. The dispersed-phase volume fraction ϕ and the surfactant mole fraction X_s are related by $X_s = A\phi/B\phi + C(1-\phi)$, where $A = M_{C_{10}D_{22}}/\rho_{C_{10}D_{22}}$, $B = (1+\omega)A$, and $C = ((M_{AOT}/\rho_{AOT}) + (M_{D_2O}/\rho_{D_2O})\omega)$. Here M_x is the molecular weight and ρ_x is the mass density of component x, and ω is the water to surfactant molar ratio.
21. Bevington, P. R., "Data Reduction and Error Analysis for the Physical Sciences," McGraw-Hill Book Company, New York, 1969.
22. Landolt-Bornstein, *in* "Zahlenwerte und funktionen," Springer, Berlin, 1962.
23. Safran, S. A., to be published *in* "Modern Amphiphilic Physics" (A. Ben-Shaul, W. Gelbart, and D. Roux, Eds.).
24. In Safran's original derivation, he ignored the finite CMC value, i.e., assuming $\phi_0 = 0$. This is a reasonable simplification for systems with very small CMC. In our case, however, in order to obtain a good fit, we have to replace ϕ by $\phi - \phi_0$, where ϕ_0 is calculated from the known CMC value of AOT.
25. Farago, B., Richter, D., Huang, J. S., Safran, S. A., and Milner, S. T., *Phys. Rev. Lett.* **65,** 3348 (1990).
26. Lovesey, S. W., and Schofield, P., *J. Phys. C: Solid State Phys.* **9,** 2843 (1976).
27. Stauffer, D., and Kiang, C. S., *Adv. Colloid Interface Sci.* **7,** 103 (1977).
28. Langer, J. S., *Lect. Notes Phys.* **132,** 12 (1980).
29. Helfrich, W., *J. Phys.* **47,** 321 (1986).
30. Kitahara, A., Kobayashi, T., and Tachibana, T., *J. Phys. Chem.* **66,** 363 (1962).